Accurate ray-tracing optical model for coded aperture spectral snapshot imagers

Antoine Rouxel, Antoine Monmayrant, Simon Lacroix, Henri Camon, Sébastien Lopez

Accurate ray tracing optical model for coded aperture spectral snapshot imagers

ANTOINE ROUXEL[1], ANTOINE MONMAYRANT[1], SIMON LACROIX[1], HENRI CAMON[1], AND SÉBASTIEN LOPEZ[2]

[1] *LAAS-CNRS, Université de Toulouse, 7 avenue du Colonel Roche, 31400,Toulouse, France*
[2] *Airbus Defence and Space, 31 rue des cosmonautes, 31400, Toulouse, France*
[*] *arouxel@laas.fr*

Compiled February 23, 2024

The image formation in coded aperture spectral imagers is a key information to process the acquired compress data, and the optical system design and calibration of these instruments require great care. We propose an analytical model for CASSI systems that builds upon ray-tracing equations of each optical component. The model takes into account optical distortions, sampling effects and optical misalignments, and allows accurate modelling and fast calibration. Numerical comparisons with the simpler model usually exploited in the literature are provided, and an experimental validation is presented.

http://dx.doi.org/10.1364/ao.XX.XXXXXX

1. INTRODUCTION

Hyperspectral imaging has been considerably renewed by the advent of coded aperture imagers, known as CASSI systems ("Coded-aperture Spectral Snapshot Imager" [1]). Unlike traditional spectral imagers where spectral bands are measured one at a time, CASSI systems measure linear combinations of spectral bands. This combination results from spatio-spectral filtering of the scene by an optical system containing one or more dispersive elements and a spatial light modulator that defines a coded aperture.

Various CASSI architectures have been proposed in the literature, with variations on the number and position of dispersive elements, the number of cameras, the nature and position of the coded aperture [2]. Whatever the optical architecture and the processing algorithms are, the extraction of relevant information from the measurements requires an accurate model of the image formation, that takes into account both the characteristics of the optical components and the sampling effects at the coded aperture and detector planes. This model plays a key role in linking the coded aperture pattern to the resulting spatio-spectral filtering occurring at the coded aperture plane, and hence on the information acquired in the encoded images. Furthermore, a realistic model is needed to simulate acquisitions, e.g. to ease the definition of the processing algorithms, or, following a co-design approach, to specify the characteristics of a system along with the processing algorithms.

Some authors consider simple models for CASSI systems [3, 4], with straightforward approximations of the spectral filtering that degrade the quality of the extracted information. Efforts have been made to improve the estimation of the spectral filtering: [5] focuses on the spatio-spectral discretization and model its impact, and [6] propose a precise spectral-dependant estimation of the point-spread function. Both works exploit a straightforward propagation model that does not consider optical distortions inherent in prism-based systems. Failing to explicitly consider these imperfections leads to artefacts in the reconstructed information, e.g. moiré effects in spectral planes, as we experienced in previous work [7]. The usual approach to account for optical distortions is to amend a simple model with experimental look-up tables (LUTs) obtained during calibration, once a prototype is built [8–10], a process that can be cumbersome and whose complexity increases with the spectral and spatial resolutions of the instrument. Calibration is deemed as one of the drawbacks of coded aperture hyperspectral imaging systems [11, 12].

We propose here an accurate *analytical model* of a CASSI system, that builds upon ray-tracing equations of each optical component. The model embraces optical distortions that are seldom considered in the literature (smile and stretching distortions) and also accounts for optical misalignments. It precisely represents the image formation process, and more specifically the spatial/spectral filtering in CASSI systems.

Besides, the advantages of an analytical model as compared to an experimental LUT are threefold. First, the model allows easy and fast calibration of CASSI prototypes, using a small set of calibration scenes to estimate the model physical parameters with an optimisation process. Second, by explicating the impact of the system physical parameters in its formulation, it

allows to dimension the system to reach given requirements, allowing fast parametric studies. And finally, it allows to easily develop a coded-image generation simulator (we provide such a simulator in [13]). Our work is complementary to [5] and [6] as it includes a high-order discretization and an estimation of the point-spread function, but also includes a modular, differentiable and realistic optical propagation model. Its differentiability is key for efficient optimisation, including machine learning approaches. The simulator thus generates realistic encoded images and yields the possibility to jointly define and configure the system and data processing algorithms along a co-design paradigm, or to train inference models on synthetic data.

Paper outline: the next section recalls the principle of a single-disperser CASSI system, and then describes two optical models: the simplified model commonly used in the literature, and the proposed analytical model. Section 3 compares both models in relation to the very accurate results provided by the optical design software Zemax, and show drastic improvements provided by our model. In section 4, we estimate the model parameters of a prototype CASSI system, depict the spectral sampling defined by our model, and provide an experimental validation. Finally, section 5 shows how the non-regular local spectral sampling induced by the distortions and discretization effects can be harnessed to enhance the spectral resolution of homogeneous regions in the scene.

2. MODEL OF A SINGLE DISPERSER CASSI

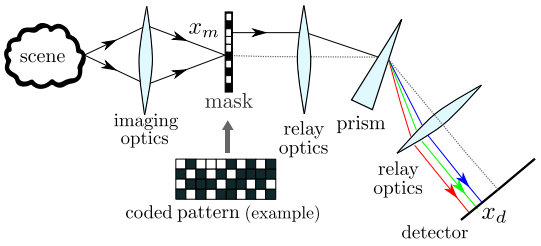

Fig. 1. Single-disperser CASSI architecture.

The studied architecture is a single-disperser prism-based CASSI (SD-CASSI), originally proposed in [1] and depicted in figure 1. Imaging optics are used to image the scene in the mask plane of the instrument. A mask placed in this plane applies a spatial modulation to the object according to a chosen coding pattern. The masked object is then imaged in the detector plane by an optical system containing relay optics and a prism, resulting in each wavelength forming on the detector a laterally shifted image. As a result, the spatial information and the spectral information from the observed object are multiplexed on the detector.

We focus throughout the paper on a prism-based SD-CASSI system, but a similar approach can be trivially applied to a grating-based SD-CASSI. Also, the proposed model can describe a dual-disperser CASSI sytem (DD-CASSI), by using it twice: once for each of the two arms of the DD-CASSI.

A. Classical propagation model

The acquisition model widely used in the literature for an SD-CASSI describes the intensity collected on the detector at the (x_d, y_d) position as:

$$I(x_d, y_d) = \int H(x_d, y_d) S_0(x_d, y_d, \lambda)\, d\lambda \qquad \textbf{(1)}$$

where H is the filtering function, (x_d, y_d) the coordinates in the detector plane, λ the wavelength of interest and S_o the spectro-spatial power density of the scene.

For the sake of simplicity, we assume the optical elements and detector to be 100 % efficient: spectral filtering only occurs in the mask plane. In the models proposed by [4, 5, 14, 15], H is written as:

$$H(x_d, y_d, \lambda) = T(x_m, y_m) \quad \text{with} \quad M_c : \begin{cases} x_m = -x_d + \Omega(\lambda) \\ y_m = -y_d \end{cases} \qquad \textbf{(2)}$$

where the "classical" model M_c is the backward propagation model mapping positions (x_d, y_d) in the detector plane to positions (x_m, y_m) in the mask plane, $T(x_m, y_m)$ is the transmission efficiency of the mask at position (x_m, y_m), independent of the wavelength λ, and the spectral spread function $\Omega(\lambda)$ models the spatial shift due to the spectral dispersion of the prism.

The underlying assumptions of the propagation model M_c are the following:

- ◇ **assumption H1**: The spectral dispersion induced by the prism is the same for all positions (x_d, y_d) in the detector plane.
- ◇ **assumption H2**: Whatever the wavelength, the magnification G_x between the detector plane and the mask plane is constant in the dispersion direction x.
- ◇ **assumption H3**: Whatever the wavelength, the magnification G_y between the detector plane and the mask plane is constant in the direction perpendicular to the dispersion y.

The assumption **H1** is contained in the function $\Omega(\lambda)$ that only depends on the considered wavelength λ and not on the position (x_d, y_d). The assumptions **H2** and **H3** are implicitly contained in the $\times(-1)$ factors in eq. Eq. (2) that correspond to $G_x = G_y = -1$.

B. Accurate propagation model

Our experimental observations [16] and simulations with the Zemax software detailed in section A indicate that the range of validity of the previous assumptions is limited. A more general propagation model is needed, that captures the specificities of a real prism-based CASSI system, such as geometric distortions induced by the prism and alignment errors. We define here the improved backward propagation model M_p, by integrating the parametrization of elementary transformations induced by the optical components (prism and lenses) and their relative orientations (rotation matrices).

B.1. Components models

From the detector back to the mask plane, light undergoes three transformations corresponding to the three optical components: a position-to-angle conversion $l_{p,a}$ through the first lens, an angle-to-angle conversion $p_{a,a}$ through the prism, and an angle-to-position conversion $l_{a,p}$ through the second lens.

Lens model $l_{p,a}$ (image plane to Fourier plane)

We assume the lenses are perfect thin lenses and the propagation distances before and after the lens are perfectly equal to their focal length F. When propagating from an image plane to a Fourier plane, such a lens performs a perfect position-to-angle conversion depending only on its focal length F, as depicted in figure 2.

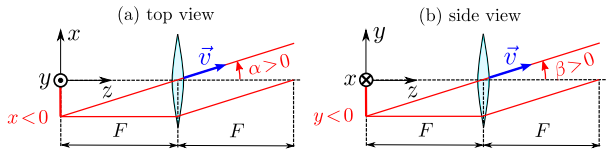

Fig. 2. Position-to-angle conversion $l_{p,a}$ induced by a perfect thin lens between object and Fourier planes.

This assumption is well verified in practice when using achromatic lenses and working with a small aperture system. This position-to-angle relation is:

$$l_{p,a} : \begin{cases} \alpha = -\arctan(x/F) \\ \beta = -\arctan(y/F) \end{cases} \quad (3)$$

where F is the focal length, (x, y) the horizontal and vertical incoming positions in the object plane and (α, β) the horizontal and vertical outgoing angles after the lens.

In terms of normalized wave-vector $\vec{v} = \vec{k} \times \frac{\lambda}{2\pi}$, after the lens, the model $l_{p,a}$ gives:

$$\begin{bmatrix} v_x \\ v_y \\ v_z \end{bmatrix} = \frac{1}{\sqrt{1+\tan^2(\alpha)+\tan^2(\beta)}} \begin{bmatrix} \tan(\alpha) \\ \tan(\beta) \\ 1 \end{bmatrix} \quad (4)$$

Lens model $l_{a,p}$ (Fourier plane to image plane)

Conversely, when propagating from a Fourier plane to an image plane, a perfect thin lens performs an angle-to-position conversion as depicted in figure 3.

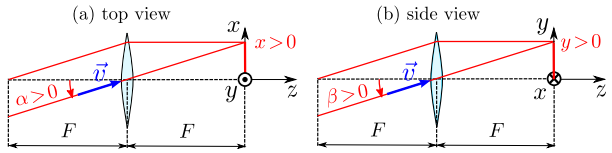

Fig. 3. Angle-to-position conversion $l_{a,p}$ induced by a perfect thin lens between Fourier and image planes.

This position-to-angle relation is:

$$l_{a,p} : \begin{cases} x = F\tan(\alpha) \\ y = F\tan(\beta) \end{cases} \quad (5)$$

where F is the focal length, (α, β) the horizontal and vertical incoming angles and (x, y) the horizontal and vertical positions in the image plane after the lens.

Note that using these definitions of $l_{p,a}$ and $l_{a,p}$ ensures that a $4F$ telescope, described by $l_{p,a} \circ l_{a,p}$ has the expected magnification ratio of $G_x = G_y = -1$.

Prism model $p_{a,a}$ (spectral deviation)

Prisms perform an angle-to-angle conversion that depends on the wavelength. We describe the incident wavevector $\vec{k}_i$ as:

$$\vec{k}_i = \frac{2\pi}{\lambda} \times \vec{v}_i$$

where the normalized vector $\vec{v}_i$ can be written as:

$$\begin{bmatrix} v_{i,x} \\ v_{i,y} \\ v_{i,z} \end{bmatrix} = \frac{1}{\sqrt{1+\tan^2(\alpha_i)+\tan^2(\beta_i)}} \begin{bmatrix} \tan(\alpha_i) \\ \tan(\beta_i) \\ 1 \end{bmatrix} \quad (6)$$

with α and β corresponding to incident angles on the input interface of the prism P expressed in the corresponding frame $\{R_{P_i}\}$, as illustrated in figure 4. Note that α_i and α_o belong to the xOz plane and β_i and β_o belong to the yOz plane of the respective frames.

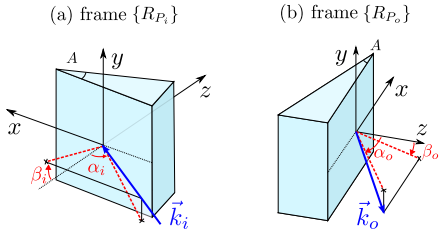

Fig. 4. Propagation of a wavevector through a prism. $\vec{k}_i$ is an incident wavevector on the input interface of the prism in the $\{R_{P_i}\}$ frame; $\vec{k}_o$ is the corresponding output vector in frame $\{R_{P_o}\}$.

The refraction law ensures that the component of the wavevector lying in the air/glass interface (i.e. component within the $z = 0$ plane in $\{R_{P_i}\}$) is conserved. The same applies to its normalized vector $\vec{v}_i$. Combining this conservation of in-plane components at both input and output interfaces with the fact that the normalized wavevector norm is 1 out of the prism and $n(\lambda)$ inside the prism, one can express the components of the output vector $\vec{v}_o$ in the $\{R_{P_o}\}$ frame as:

$$\begin{bmatrix} v_{ox} \\ v_{oy} \\ v_{oz} \end{bmatrix} = \begin{bmatrix} \cos(A)v_{ix} - \sin(A)\sqrt{[n(\lambda)]^2 - v_{ix}^2 - v_{iy}^2} \\ v_{iy} \\ \sqrt{\|\vec{v}_o\|^2 - v_{ox}^2 - v_{oy}^2} \end{bmatrix} \quad (7)$$

where A is the apex angle of the prism, $\|\vec{v}_o\| = 1$, the norm of the $\vec{v}_o$ vector, λ the considered wavelength and $n(\lambda)$ the corresponding refractive index.

Output angles in the frame of the output face $\{R_{P_o}\}$ can be expressed with vector $\vec{v}_o$ components as:

$$p_{a,a} : \begin{cases} \alpha_o = \arctan(v_{ox}/v_{oz}) \\ \beta_o = \arctan(v_{oy}/v_{oz}) \end{cases} \quad (8)$$

Combining equations Eq. (8), Eq. (7) and Eq. (6) defines the analytical model $p_{a,a}$, giving a closed-form expression of α_o and β_o as a function of α_i and β_i. This expression is somewhat complex, it is not presented here explicitly (see the code in [13] for more details on the exact implementation). For a grating-based SD-CASSI, a similar approach can be derived to define an analytic model for wavelength dependent ray deviation [17].

B.2. $\mathbf{M_p}$ *: combination of elementary models*

The model M_p describes the propagation from a position (x_d, y_d) at wavelength λ through two lenses and a prism as illustrated in figure 5. The optical layout is such that the optical axis of the lenses L_1 and L_2 corresponds to the minimum deflection of the prism for the central wavelength of the system. The latter is a design choice made with respect to the spectral range of the instrument.

The full model M_p is defined by the composition of the elementary transformations $l_{p,a}$, $p_{a,a}$ and $l_{a,p}$:

$$\begin{aligned} M_p &: (x_d, y_d, \lambda) \to (x_m, y_m, \lambda) \\ M_p &= l_{a,p} \circ R_{P_o \to L_1} \circ p_{a,a} \circ R_{L_2 \to P_i} \circ l_{p,a} \end{aligned} \quad (9)$$

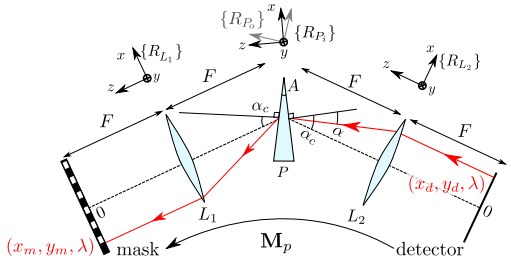

Fig. 5. The backward propagation model M_p is the combination of the elementary transformations $l_{p,a}$, $p_{a,a}$ and $l_{a,p}$ and the rotation operators $R_{L_2 \to P_i}$ and $R_{P_o \to L_1}$.

with $R_{L_2 \to P_i}$ and $R_{P_o \to L_1}$ the rotation operators associated respectively with the change of reference frame between $\{R_{L_2}\}$ and $\{R_{P_i}\}$, and between $\{R_{P_o}\}$ and $\{R_{L_1}\}$ (see figure 5).

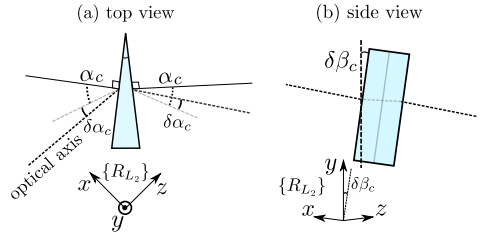

Fig. 6. Prism alignment parameters. The angle α_c is the angle of incidence corresponding to the minimum deflection of the prism at the central wavelength. The angles $\delta\alpha_c$ and $\delta\beta_c$ describe small errors of alignment respectively with respect to the minimum deflection and with respect to the verticality of the prism.

These two operators are parametrized according to the optomechanics on which the prism is fixed. To allow the alignment of the optical system, it is generally necessary to have at least two degrees of freedom on this component. A rotation around the y-axis, illustrated in figure 6, allows the positioning around the minimum of deflection, and a rotation around the x-axis guarantees the verticality of the prism. To account for alignment errors, we have parametrized these two rotations by $\delta\alpha_c$ and $\delta\beta_c$, which represent respectively the error from the incidence α_c corresponding to the minimum of deviation and the error from the vertical (see figure 6). To summarize, our model parameters are the focal length F, the apex angle A, the angle of incidence on the prism α_c ensuring minimum deflection at λ_c, and the two angles $\delta\alpha_c$ and $\delta\beta_c$ that define the alignment errors of the prism.

C. Discussions on dispersive elements

In the literature, there has been several discussions on which optical component to use for spectral dispersion.

One commonly employed element is the grating, in transmission or reflection, renowned for its linear dispersion capabilities. However, its utility is somewhat constrained by a relatively narrow spectral range, beyond which its efficiency notably diminishes. Moreover, going beyond one octave requires special care to avoid diffraction orders overlapping.

Conversely, prisms offer a broader spectral range with high efficiency, but at the expense of introducing distortions. These include smile and stretching effects, alongside inherent nonlinear dispersion, which can complicate the interpretation of raw spectral images.

An alternative is the Amici prism [18], a composite of three prisms arranged to combine the benefits of both grating and prism. It achieves linear dispersion over an extensive spectral range, akin to gratings, while retaining the wide-range applicability of prisms [19]. Despite its merits, the Amici prism is not without drawbacks, as it still manifests smile and stretching distortions.

In this article, we chose to focus on the prism as it induces various optical distortions that need to be addressed, and is also the basic building block of the Amici prisms. Note that a grating model is also included in our associated simulator [13].

3. NUMERICAL VALIDATION

To quantify the advantages of the model M_p over the classical model M_c, both were compared to simulations performed by the optical design software Zemax. Zemax was chosen as the reference for the evaluation because it is widely used in the optical systems industry.

The simulated system is an SD-CASSI as depicted in figure 5. We first assume that there is no misalignment ($\delta\alpha_c = \delta\beta_c = 0$) and simulate in Zemax the propagation of a grid of 19×19 points, forming a field of view of $8 \times 8\,\text{mm}^2$, from the detector plane to the mask plane (see figure 7). The spectral range

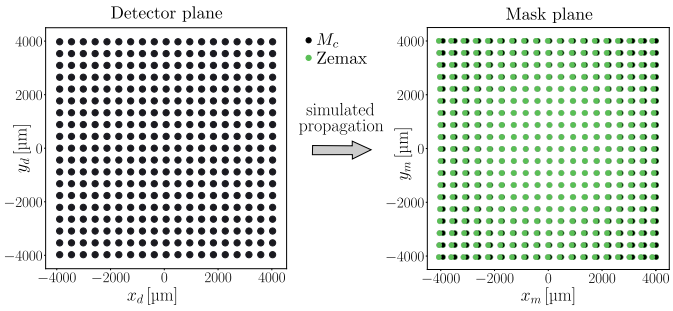

Fig. 7. Typical comparison: a regular grid of 19×19 points in the detector plane (top) is propagated to the mask plane (bottom) with both the M_c model (black dots) and Zemax (green dots).

evaluated is the visible and near-infrared $[450 - 780]$ nm. The lenses are perfect, with focal length $F = 165$ mm, and the prism is equilateral ($A = 60°$) in BK7 (these parameters are those of the prototype presented in section A, except the field of view which is larger, so as to better exhibit the differences between the models). The central wavelength is fixed at $\lambda_c = 532$ nm, and the associated minimum deviation D_m is calculated by direct application of the Snell-Descartes law [20]:

$$D_m = 2\arcsin(n(\lambda_c)\sin(A/2)) - A \tag{10}$$

where $n(\lambda_c)$ is the refractive index of the prism at the central wavelength and A the apex angle of the prism. We finally get the angle of incidence on the prism α_c:

$$\alpha_c = \frac{A + D_m}{2} \tag{11}$$

In our case, $\alpha_c = 49.44°$. Since the misalignments cannot be taken into account by the classical model we first assume that they are non-existent. In the last validation step, we perform a comparison between our model and the Zemax simulations with increasing misalignments.

A. Evaluation of the classical model M_c

Preliminary methodological note: The M_c model assumes identical spectral dispersion for all positions in the field of view (**assumption H1**, section A). The Ω function related to the dispersion thus depends only on the wavelength λ. Different ways of evaluating this dispersion have been proposed in the literature [7, 11, 14]. To avoid any bias due to the use of an inadequate model for Ω, we extrapolate this function from the Zemax reference simulation with a polynomial of degree 10. We obtain a dispersion function for the point at the centre of the detector $(x_d, y_d) = (0, 0)$. This function faithfully reproduces the spatial shifts observed at the mask for the different wavelengths.

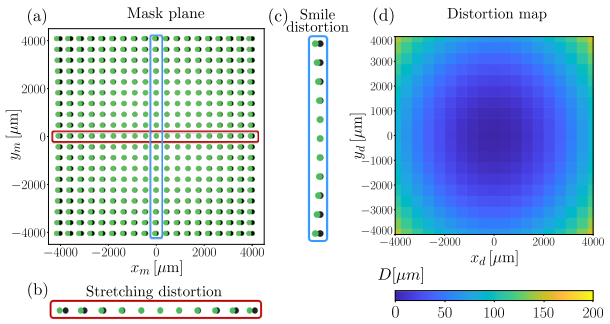

Fig. 8. Comparison between Zemax and M_c propagation models for the central wavelength $\lambda = 532$ nm: (a) points in the mask plane (x_m, y_m) predicted by M_c (black) and by Zemax (green); (b) zoom on the stretching distortion along the horizontal axis x; (c) zoom on the smile distortion along the vertical axis y; (d) geometric distortions mapped on detector points: Euclidean distance D between points predicted by Zemax and M_c.

Figure 8 (a) shows the points propagated by Zemax (black dots) and by the M_c model (green dots) for the wavelength $\lambda = 532$ nm. The M_c model is accurate around the centre of the field of view but the error increases with the distance from the centre. One can see different geometric distortions along the x and y axes.

Let us observe more precisely what happens along the x axis with the zoom in figure 8 (b): all the black points are to the right of the corresponding green points. This is due to the non-linear deviation of the prism around its minimum of deviation, which induces a geometric distortion that we call *stretching distortion* as the horizontal magnification G_x changes with the position. Since the classical model M_c assumes a constant magnification G_x across the field of view (**assumption H2**), it does not properly account for this stretching distortion.

Along the vertical axis y, after propagation, the vertical lines are bowed, as illustrated in figure 8 (c). This is the *smile distortion*, well known in spectroscopy. It couples the horizontal position x_m in the mask plane to the vertical position y_d in the detector plane. As the classical model M_c treats both directions independently (see eq. Eq. (2)), it cannot account for smile distortion.

For a more quantitative analysis of the differences between Zemax and M_c, we present in figure 8 (d) the distortion map, i.e. the Euclidean distance D between the corresponding black and green points. Note that distortion values D are plotted as a function of the originating position in the detector plane (x_d, y_d) to allow easier comparison between considered wavelengths. We can see that this distance D grows with the radial distance to the centre of the field of view, reaching up to 190 µm in the corners. For comparison, the typical size of a mirror of a digital micro-mirror device (DMD) typically used as a mask is of the order of 5 µm. This distance thus corresponds to a maximum error of around 38 micro-mirrors on a typical DMD.

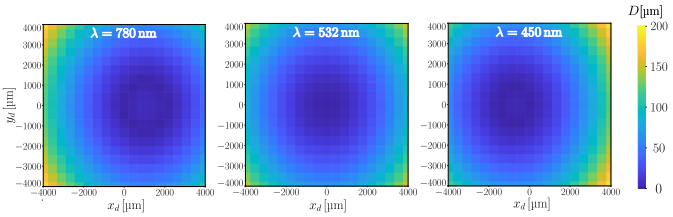

Fig. 9. Distance maps comparing the classical M_c model to Zemax for (left) upper, (centre) central and (right) lower wavelengths.

Let us now observe the wavelength dependence of these geometric distortions. As a reminder, the prism is positioned so that the centre of the field of view is at the minimum of deviation for $\lambda_c = 532$ nm. The distortion maps presented in figure 9 correspond to this configuration for three wavelengths: 450, 532 and 780 nm. One can see that they are off-centred and reach higher values for wavelengths lower (450 nm) and higher (780 nm) than the central wavelength. Indeed, for both these wavelengths, we are no longer at the minimum of deviation where the geometric distortions are minimal.

This can also be observed in figure 10, in which histograms of the distances D for the 19×19 points of the field of view are plotted for three wavelengths: 450 nm, 532 nm and 780 nm. For each of these wavelengths, the dotted lines indicate the 95$^{\text{th}}$ percentile of D. By definition, 95% of the values of D lie below the 95$^{\text{th}}$ percentile, which is therefore a relevant scalar metric to assess the differences between the two models. We observe a higher 95$^{\text{th}}$ percentile of D for $\lambda = 450$ and 780 nm (respectively 136 and 133 µm) than for the central wavelength $\lambda_c = 532$ (116 µm). The classical model tends here to produce significant positioning errors, of the order of 25 micro-mirrors for a typical DMD.

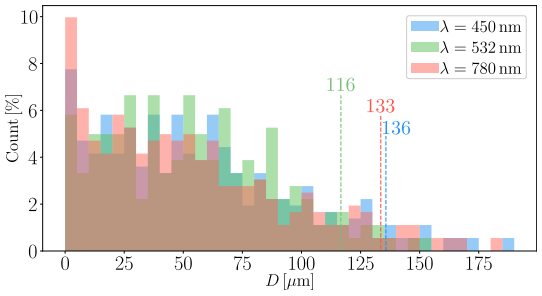

Fig. 10. Histogram of Euclidean distance D between points propagated into the mask plane with Zemax and the with classical model M_c for lower, central, and upper wavelengths. For each wavelength, the dashed line corresponds to the distance of the 95$^{\text{th}}$ percentile (i.e. 95% of the distances are below this limit).

B. Evaluation of the proposed model M_p

M_p gives the position (x_m, y_m) in the mask plane as a function of the position in the detector plane (x_d, y_d) and the considered

wavelength λ. Contrary to the classical model, the spectral dispersion induced by the prism is not the same for all positions in the field of view (no **assumption H1**). Furthermore, we make no assumptions about the magnification in the x and y directions (no **assumptions H2** and **H3**).

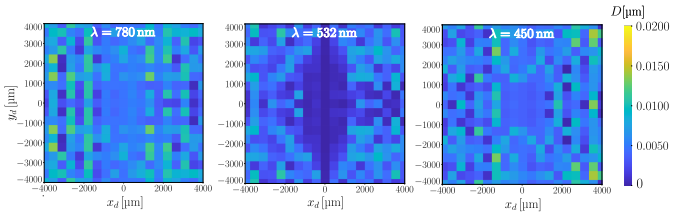

Fig. 11. Distance maps comparing the proposed M_p model to Zemax for (left) upper, (centre) central and (right) lower wavelengths.

Figure 11 presents the distortion maps obtained with the M_p model for three wavelengths, with the same metric as in section A (Euclidean distance D between image points from the M_p model and those from the Zemax simulation). Comparing the distortion maps in figures 9 and 11, one can observe a sizeable difference in the scale of the distortion in the field of view: the maximum D distance decreases from 190 µm to 0.015 µm, i.e. a reduction of about 4 orders of magnitude. Figure 11 also shows that the accuracy of the model does not depend on the wavelength.

The same trend can be observed by comparing the histograms of D presented in figure 12 and the values of the 95$^{\text{th}}$ percentile of D. These values are more than two orders of magnitude below the typical size of a micro-mirror (5 µm) and therefore correspond to negligible positioning errors.

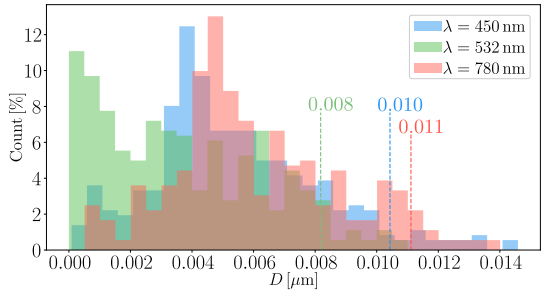

Fig. 12. Histogram of Euclidean distance D between Zemax and the proposed model M_p in the mask plane for lower, central, and upper wavelengths. For each wavelength, the dashed line corresponds to the distance of the 95$^{\text{th}}$ percentile (i.e. 95% of the distances are below this limit).

The M_p model also accounts for prism misalignments (non-zero values of $\delta\alpha_c$ and $\delta\beta_c$, see figure 6). Since they cannot be modelled by the classical M_c model, we can only compare to the Zemax simulations. Figure 13 represents the histograms of D for a series of misalignment values, starting with typical values compatible with an expected experimental alignment, and multiplying them by a factor of 3 and 10. The model M_p estimates the distortions with an accuracy similar to that obtained without misalignments (compare to figure 12), even for large misalignments: the slight variations observed between the values of the 95$^{\text{th}}$ percentiles for the various misalignment values are not significant.

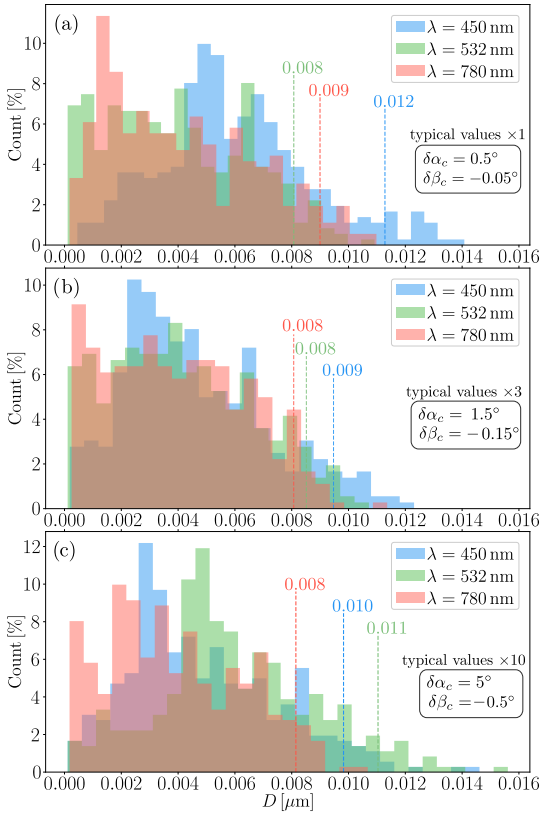

Fig. 13. Histograms of Euclidean distances D between the Zemax simulations and the M_p model, with increasing misalignment, for three wavelengths. In dotted line, the 95$^{\text{th}}$ percentile of D.

4. EXPERIMENTAL VALIDATION

We present in this section a validation of the proposed model M_p with a prototype SD-CASSI system. The model parameters are first determined with a calibration process, and the spectral sampling defined by the model is validated by observing a known spectrum.

A. Geometric spatio-spectral calibration of an SD-CASSI system

One of the benefits of a parametric model of the image formation is that it allows a quick calibration, using only a few images of a known geometric pattern and an optimisation technique. This is more straightforward than building an experimental LUT for each individual pixel, which is reckoned as a laborious process in the literature [11, 12, 21], even though efficient approaches have been proposed [22]. Also, while buidling experimental LUTs is tractable for low spectral and/or spatial resolution, the process becomes more difficult and time consuming for high resolution imagers.

The proposed model-based calibration approach pertains to the *geometry* of an SD-CASSI system, as expressed by the model M_p: we do not consider purely photometric phenomena (quantum efficiency and vignetting).

The principle of the calibration is to fit the M_p model parameters to real measurements with a non-linear least-square optimisation. For this purpose, we rely on the association of features of known positions (x_m, y_m) in the scene to pixel coordinates (x_d, y_d) in the detector, for a series of wavelengths

λ. We use the DMD as the scene, displaying a chequerboard pattern, which defines easily detectable corners on the image formed in the detector plane (figure 14). The corners are detected with the OpenCV image processing library.

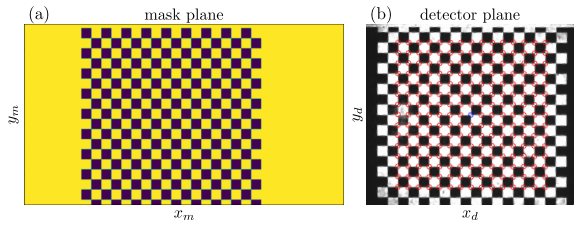

Fig. 14. Calibration pattern on the DMD at the scene (a), and extracted corners in the detector plane (b).

Our SD-CASSI prototype is composed of two lenses, two folding mirrors, one prism, a matrix of micro-mirrors acting as a programmable mask, and a CMOS camera (figure 15). The

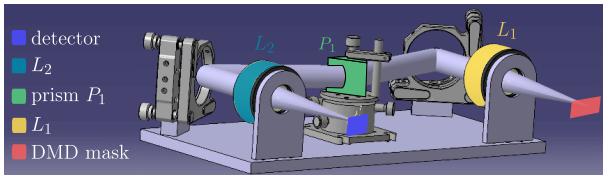

Fig. 15. 3D model of the prototype.

folding mirrors have no contribution to the propagation model, they just ensure easier alignment and reduced volume of the optical system. The input scene in the object plane of the system is 3.5×3.5 mm^2 wide, and spectrally ranges from 450 to 750 nm. The components of the prototype are described table 1.

Component	Type and characteristics
Lenses (L_1, L_2)	Thorlabs TTL165-A, achromatic over $[450 - 780]$ nm, $F = 165$ mm
Prism (P_1)	BK7 material, equilateral, apex angle $A = 60°$
DMD	Texas Instruments DLP3010, 720×1280 square 5.4 µm micro-mirrors, defining a 3.9×6.9 mm^2 mask
Detector	The Imaging Source, 33UP2000, 1920×1200 4.8 µm pixels

Table 1. Characteristics of the prototype components

We experimentally estimated the system point spread function (PSF): it slightly changes with the position in the field of view and wavelength, and its diameter is bounded by 15 µm.

The calibration chequerboard pattern is made up by 17×17 square regions of 30×30 mirrors, which defines 289 corners. Three lasers are used to illuminate the chequerboard pattern, with respective wavelengths 450, 532 and 780 nm. In total, $3 \times 289 = 867$ $(x_d, y_d, x_m, y_m, \lambda)$ quintuplets are provided to the non-linear least-square regression process to estimate the parameters that define the M_p model. As a reminder, these parameters are the focal length F, the apex angle A, the angle of incidence on the prism α_c ensuring minimum deflection at λ_c, and the two angles $\delta\alpha_c$ and $\delta\beta_c$ that define the alignment errors of the prism.

The estimated parameters are given in Table 2 with the associated 95 % confidence interval obtained with a jackknife resampling. According to the components' specifications, the focal lengths F and apex angle A may respectively vary by 1 % and 0.1 % around their specified values of 165 mm and 60°: the estimated values are within these bounds. The minimum of deviation is also extremely close to the expected value. As for $\delta\alpha_c$ and $\delta\beta_c$, the estimated values are coherent with the precision of the experimental alignment. In particular, as verticality of the prism is easier to assess than its orientation with respect to the minimum of deviation, it is not surprising that $|\delta\beta_c|$ is smaller than $|\delta\alpha_c|$.

	F [µm]	A [°]	α_c [°]	$\delta\alpha_c$ [°]	$\delta\beta_c$ [°]
Value	165 449	60.0005	49.4416	0.5778	−0.1407
C.I.	26	0.0098	0.0134	0.312	0.092

Table 2. Calibration results: value estimated for the parameters and associated 95 % confidence interval (C.I.).

An alternate way to assess the quality of the calibration is to calculate the reprojection error, *i.e.* the Euclidean distance D between the extracted corner positions and the ones predicted using the model with the estimated parameters. The values of D plotted as a function of the original position in the image plane are reported in figure 16, and the associated histograms are plotted in figure 17, with the distance of the 95$^{\text{th}}$ percentile for the three reference wavelengths. For 95% of the points in the field of view, the reprojection errors do not exceed 6.9 µm for the upper wavelength, 10.7 µm for the central wavelength and 8.4 µm for the lower wavelength.

These errors are significantly larger than the ones obtained with the numerical projections presented in section 3. This comes from various experimental causes. In particular, the lasers used for the calibration have spectral FWHM of the order of 0.5 nm, are not thermally regulated and exhibit a temperature drift of the order of 0.2 nm/°C, resulting in an uncertainty on the exact position on the detector of more than one pixel ($\gtrsim$ 4.8 µm) Additionally, the detector 4.8 µm sampling step and the experimentally measured PSF of 15 µm diameter affects the precision of the corners detection. Nevertheless, these errors are sub-PSF and correspond to a rather accurate spatio-spectral calibration of the SD-CASSI.

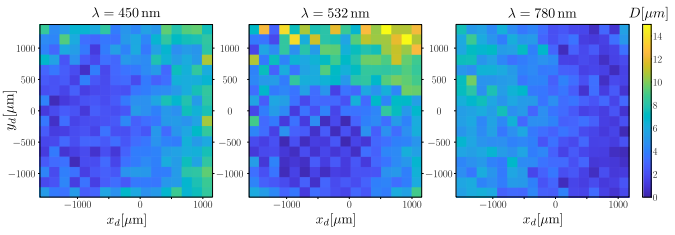

Fig. 16. Experimental reprojection error D for the 3 reference wavelengths.

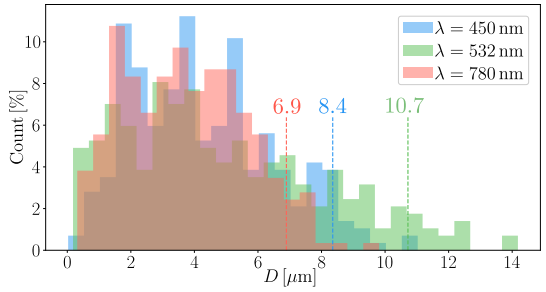

Fig. 17. Histogram of the reprojection error D for the 3 reference wavelengths. For each wavelength, the color dashed line corresponds to the distance of the 95th percentile.

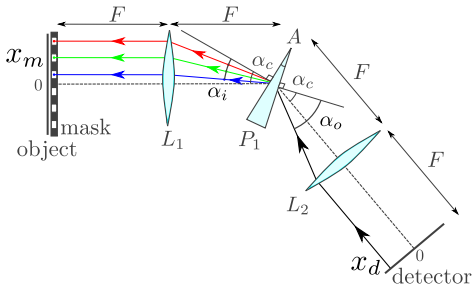

Fig. 18. The spectral sampling at each pixel in the detector plane depends on the back-propagation to the mask micro-mirror centres.

B. Estimation of the spectral sampling

To evaluate the spectral sampling of an SD-CASSI or a DD-CASSI system, one usually resort to a an experimental LUT-based calibration [5, 11, 12, 23, 24]. The proposed method relies on the 5-parameter model estimated in section A to calculate the spectral sampling specific to each pixel, without any additional measurement.

As illustrated in figure 18, for any given image pixel (x_d, y_d), with the analytical model M_p one can back propagate light into the mask plane to determine which micro-mirrors can send light at that pixel position. In the mask plane, the light from the pixel would form an horizontal rainbow line, spread over several adjacent micro-mirrors. The wavelengths corresponding to the centre of each of these micro-mirrors define the spectral sampling that the DMD is imposing on the considered pixel. Due to the non-linear dispersion, the smile distortion and the stretch distortion, this sampling differs for each pixel in the detector plane. We thus call it the *local spectral sampling*. The entire process to determine the local spectral sampling can be summarized in three steps:

1. from the position (x_d, y_d) of the pixel in the detector plane, one determines the angles (α_o, β_o) on the back side of the prism using the lens model $l_{p,a}$;

2. from the position (x_m, y_m) of a given micro-mirror in the mask plane, one determines the angles (α_i, β_i) on the front side of the prism using the lens model $l_{a,p}$;

3. using the prism model $p_{a,a}$, one determines whether there is a wavelength λ such that (α_i, β_i) corresponds to (α_o, β_o) thanks to the deflection induced by the prism. This corresponds to finding the value of $n(\lambda)$ that solves the equation 7.

If such a wavelength exists, it is part of the local spectral sampling of the considered pixel. If it doesn't, it means this particular micro-mirror does not influence the light impinging on the pixel. The local spectral sampling for this pixel is fully defined when all the micro-mirrors have been tested. Once this procedure has been applied to all the pixels of the detector, we have the local spectral sampling for the whole detector, together with the link between each micro-mirror and the spectral samples it controls over various pixels in the detector.

Of course, in practice, we do not test every single micro-mirror and every possible wavelength in the spectral range of interest for each pixel of the detector, as it is prohibitively time-consuming. Some considerations can be used to significantly reduce the micro-mirrors to test for any given pixel. In particular, as the device is mostly line-independent, for each pixel, we can limit the test to a single line of micro-mirrors. Moreover, for each pixel, it is easy and fast to back propagate the two extreme wavelengths of the spectral range of interest, thus bounding the lateral positions of the micro-mirrors to test on the DMD. Note that once the 5 physical parameters of the model are known, all these pixel-dependant spectral samplings can be pre-computed for spectral reconstruction or any other interpretation or processing of the encoded images.

C. Experimental validation of the local spectral sampling

The spectral calibration obtained using the local spectral sampling is tested using a fluorescent lamp that illuminates the object and mask planes homogeneously. The DMD mask pattern consists of a single vertical slit, turning the SD-CASSI into a prism-based spectrometer.

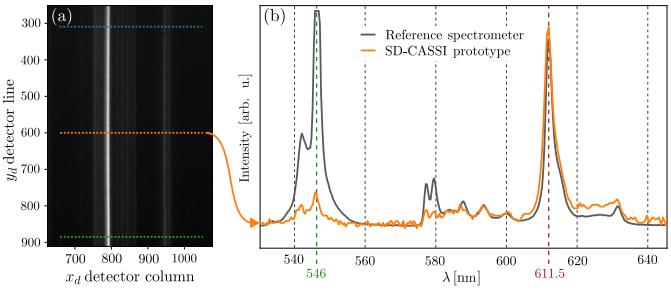

Fig. 19. Spectral calibration validation: (a) detector image for a single slit DMD mask and a uniform scene lighted by a fluorescent lamp; (b) fluorescent lamp spectrum measured with a reference spectrometer (grey line) and with the SD-CASSI using line $y_d = 600$ of the detector (orange line). Two spectral peaks at 546 nm and 611.5 nm are used for comparison.

The image formed on the detector (see figure 19 (a)) shows the different spectral lines and bands of the fluorescent lamp. Note that the dispersion is such that wavelength λ decreases with increasing x_d position on the detector (longer wavelengths are imaged on the left). Using our local spectral sampling, the intensity along any horizontal line can be calibrated in wavelength to retrieve the spectrum. Figure 19 (b) shows the spectrum obtained from the line $y_d = 600$ of the detector (orange line), together with an independent reference measurement of the spectrum of the scene (black line, obtained using a UV-VIS Ocean Optics Flame spectrometer).

We can see from this comparison that the spectral local sampling is accurate enough to precisely locate the features of the spectrum (like the peaks at 546 and 611.5 nm for ex-

ample). However, we can see significant intensity dissimilarities between the retrieved and reference spectra: this is due to the absence of intensity (or quantum efficiency) calibration on our prototype, whereas the quantum efficiency is properly accounted for in the signal from the reference spectrometer. Moreover, as it consists of a single line of pixels, the retrieved spectrum is significantly noisier than the reference spectrum obtained by collecting the light for the whole scene.

In order to ascertain the validity of the local spectral sampling, we retrieved the calibrated spectrum using several lines across the field of view. Figure 20 (a) shows typical spectra retrieved for $y_d = [310, 600, 890]$. As these spectra are almost perfectly overlapped, we shifted them vertically for better readability of the figure.

A close up on the main peak at 611.5 nm of the spectrum is shown in figure 20 (b): it reveals that although the measured spectra are perfectly consistent and correspond to the same spectral shape (give or take the acquisition noise), they are based on different spectral samples.

In this simple example of a single slit DMD pattern, recombining accurately the different lines of the detector in one single spectrum with higher signal to noise ratio requires to take this change of the spectral sampling into account.

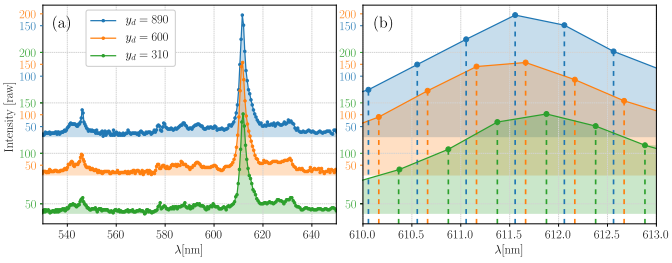

Fig. 20. Spectral calibration validation across the field of view: (a) spectra measured from three different lines of the detector ($y_d = [310, 600, 890]$) give consistent results; (b) close inspection of the spectra reveal the local spectral sampling that changes across the detector.

5. SPECTRAL SUPER-RESOLUTION

In most papers [5, 14, 15] authors assume that the data collected by CASSI systems can be interpreted with a uniform spectral sampling, thus neglecting the change observed in figure 20 (b). This assumption can simplify hyperspectral cube reconstruction, as uniform spectral sampling implies that acquired raw data conveniently consists of well-defined monochromatic planes or images. But it leads to various issues, like moiré patterns, that are particularly detrimental for high resolution CASSI imagers [7]. There has been some discussion regarding these issues [7–10, 12], but even the most effective methods, i.e correction of the filtering function H [16], result in a loss of spectral resolution by a factor of 2. Conversely, model-based calibration gives an easy access to the spectral local sampling, with no resolution losses and can be harnessed to achieve super-resolution.

Indeed, considering local spectral sampling gives the ability to achieve spectral super-resolution when several adjacent pixels share the same spectrum. Such groups of pixels, dubbed spectrally homogeneous spatial regions are fairly common and can be harnessed to speed-up hyperspectral imaging [7, 25]. To demonstrate spectral super-resolution we compare the hyperspectral measurements achieved with our SD-CASSI prototype with either a uniform or local spectral sampling, on a spectrally homogeneous scene.

The acquisition scheme is a simple moving-slit sequence: we successively open the columns of micro-mirrors on the DMD mask and record the corresponding image on the detector. The mask plane is illuminated with a large single-mode He-Ne laser beam ensuring an homogeneous spectrum across many pixels. The raw data-cube is then interpreted to retrieve the spectrum at every point in the mask plane.

The figure 21 shows the spectral sampling ((a) and (c)) and measured spectral intensities ((b) and (d)) across 7 neighbour pixels (yellow to blue color code) when using either the uniform ((a) and (b)) or local ((c) and (d)) spectral sampling.

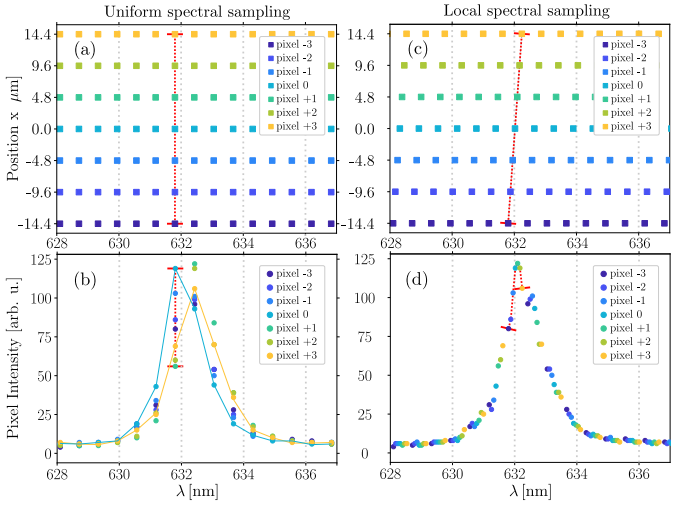

Fig. 21. Spectral super resolution of a He-Ne laser spectrum: the uniform spectral sampling ((a) & (b)) implies that adjacent pixels provide several intensity values for a single wavelength whereas the proposed approach ((c) & (d)) properly describes the minute changes in sampling and adjacent pixels provide spectral super-resolution.

With a uniform spectral sampling (see figure 21 (a)), each of the 7 pixels provides an independent measurement over the same spectral samples (see the dotted red line in figure 21 (a)). We thus obtain one spectrum per pixel (see for example the dark blue and yellow spectra in figure 21 (b), measured 6 pixels apart). We can observe a large intensity variation across these spectra (dotted red line in figure 21 (b)) and a large, regular, spectral sampling of about 0.65 nm. Similar intensity variations, forming moiré patterns, have been observed in DD-CASSI systems and require cumbersome mitigation post-processing that degrade significantly either spatial of spectral resolution of the reconstructed hyperspectral data [16], hindering the development of high resolution DD-CASSI.

Conversely, with a pixel-specific spectral sampling, the same raw data can be interpreted in a more precise and faithful way. The spectral sampling is slightly different for each pixel (see the slanted dotted red line in figure 21 (c)). We thus have access to interleaved spectral samples (see the dotted red curve in figure 21 (d)) and we can reconstruct a super-resolved spectrum for the whole region, with a sampling of about 0.09 nm. This super-resolved spectrum is irregularly but finely sampled, and measured accurately in intensity.

It is noteworthy that harnessing spectral sampling effects has been previously explored for a color-coded aperture spectral imager [26], exploiting the difference of spectral sampling between the response of the color filters and the prism dispersion. Interestingly, these are two different but complementary ways of using sampling effects: our method relies on the optical system distortions and discretization of mask and detector, while [26] harnesses the difference of spectral sampling induced by spectral filters and prism dispersion. Both approaches could in principle be combined.

6. CONCLUSION

The proposed analytical model for back-propagation in prism SD-CASSI is based on ray-tracing and simple rotation matrices, and relies on a few physical parameters directly related to the optical components properties and their alignment. It models accurately systems under design, and allows fast and easy calibration of existing prototypes. This model is part of a DD-CASSI simulator, available online as Free Open Source Software (FOSS)[13].

This model offers positioning accuracy of the propagated principal rays comparable to that of an industry standard like Zemax. However, contrary to Zemax, it is perfectly fit to be integrated into larger software ecosystems, e.g. for optimization, data processing or co-design. This enables the complete study of co-designed prototypes and companion algorithms in one unified framework. Such studies could provide meaningful insights on the interplay between opto-geometrical and algorithmic trade-offs and their impact on the overall efficiency of a particular hyperspectral measurement strategy.

Using this model to calibrate an SD-CASSI prototype, we accurately describe minute changes in the spectral sampling across the field of view, without resorting to the building of experimental LUTs. These changes are inducing spectral measurement artefacts, particularly detrimental in high-resolution CASSI systems. Access to the local spectral sampling allows to eliminate the spectral artefacts and even to exploit them to achieve super-resolved measurements.

As presented here, this model is limited to prism-based single disperser (SD) CASSI systems. However, it could be trivially extended to grating-based SD-CASSI by replacing the prism wavelength-dependent angular dispersion by that of transmission or reflection gratings. Moreover, this model is also extremely valuable for dual-disperser (DD) CASSI systems that either rely on two chained SD-CASSI (two arms) or on a double-pass in one SD-CASSI (one arm in double-pass). A key requirement with DD-CASSI is the perfect symmetry between each pass or arm: exploiting the model to simulate or calibrate independently half of the DD-CASSI system would provide hints on the impact of misalignment and dissymmetry on the achievable performance.

In addition, this model could be complemented by a an estimate of the spectral quantum efficiency over the field of view, as well as precise estimate of the spectrally-dependant PSF, as proposed in [6]. Moreover, it could also account for the diffraction induced by the DMD, as was done in [27]. Finally, in order to take into account defocussing at the different relay and imaging planes together with non-paraxial lens aberrations, the perfect lens model could be replaced by a proxy model of some specific real lens or lens assembly, as proposed in [28].

Data availability. Data underlying the results presented in this paper are not publicly available at this time but may be obtained from the authors upon reasonable request.

REFERENCES

1. A. Wagadarikar, T. John, R. Willett, and D. Brady, "Single disperser design for coded aperture snapshot spectral imaging," Appl. Opt. **47**, B44–B51 (2008).
2. X. Cao, T. Yue, X. Lin, *et al.*, "Computational snapshot multispectral cameras: Toward dynamic capture of the spectral world," IEEE Signal Process. Mag. **33**, 95–108 (2016).
3. I. Ardi, H. Carfantan, S. Lacroix, and A. Monmayrant, "Fast hyperspectral cube reconstruction for a double disperser imager," in *2018 26th European Signal Processing Conference (EUSIPCO),* (IEEE, 2018).
4. N. Diaz, J. Ramirez, E. Vera, and H. Arguello, "Adaptive multisensor acquisition via spatial contextual information for compressive spectral image classification," IEEE J. Sel. Top. Appl. Earth Obs. Remote. Sens. **14**, 9254–9266 (2021).
5. H. Arguello, H. Rueda, Y. Wu, *et al.*, "Higher-order computational model for coded aperture spectral imaging," Appl. Opt. **52**, D12 (2013).
6. L. Song, L. Wang, M. H. Kim, and H. Huang, "High-accuracy image formation model for coded aperture snapshot spectral imaging," IEEE Trans. on Comput. Imaging **8**, 188–200 (2022).
7. E. Hemsley, I. Ardi, S. Lacroix, *et al.*, "Optimized coded aperture for frugal hyperspectral image recovery using a dual-disperser system," J. Opt. Soc. Am. A **37**, 1916 (2020).
8. J. Xu, B. Hu, and D. Feng, "The correction of recovered spectral images in a hadamard transform spectral imager based on a digital micro-mirror device," Appl. Spectrosc. **66**, 1044–1052 (2012).
9. J. Xu, Z. Zhu, C. Liu, and Z. Huang, "The processing method of spectral data in hadamard transforms spectral imager based on DMD," Opt. Commun. **325**, 122–128 (2014).
10. C. Ma, H. Lin, G. Zhang, and R. Du, "Digital micro-mirror device based multispectral imaging using compressed fourier spectrum," Opt. Commun. **426**, 348–358 (2018).
11. A. A. Wagadarikar, N. P. Pitsianis, X. Sun, and D. J. Brady, "Video rate spectral imaging using a coded aperture snapshot spectral imager," Opt. Express **17**, 6368 (2009).
12. P. K. Poon, "Practical considerations in experimental computational sensing," Univ. Ariz. (2016).
13. A. Rouxel and L. Paillet, "Simca," https://github.com/a-rouxel/simca (2023).
14. M. E. Gehm, R. John, D. J. Brady, *et al.*, "Single-shot compressive spectral imaging with a dual-disperser architecture," Opt. Express **15**, 14013 (2007).
15. M. Dunlop-Gray, P. K. Poon, D. Golish, *et al.*, "Experimental demonstration of an adaptive architecture for direct spectral imaging classification," Opt. Express **24**, 18307 (2016).
16. E. Hemsley, S. Lacroix, H. Carfantan, and A. Monmayrant, "Calibration of programmable spectral imager with dual disperser architecture," Opt. Commun. **468**, 125767 (2020).
17. N. Bonod and J. Neauport, "Diffraction gratings: from principles to applications in high-intensity lasers," Adv. Opt. Photonics **8**, 156 (2016).
18. N. Hagen and T. S. Tkaczyk, "Compound prism design principles, i," Appl. Opt. **50**, 4998 (2011).
19. Y. Wu, I. O. Mirza, G. R. Arce, and D. W. Prather, "Development of a digital-micromirror-device-based multishot snapshot spectral imaging system," Opt. Lett. **36**, 2692 (2011).
20. R. S. Longhurst, *Geometrical and physical optics* (Longman, London, 1973).
21. C. Deng, X. Hu, J. Suo, *et al.*, "Snapshot hyperspectral imaging via spectral basis multiplexing in fourier domain," Opt. Express **26**, 32509 (2018).
22. C. Ma, H. Lin, G. Zhang, and R. Du, "An efficient calibration method for multi-spectral imaging," Opt. Commun. **420**, 14–25 (2018).
23. G. R. Arce, D. J. Brady, L. Carin, *et al.*, "Compressive coded aperture spectral imaging: An introduction," IEEE Signal Process. Mag. **31**, 105–115 (2013).
24. N. Goldstein, P. Vujkovic-Cvijin, M. Fox, *et al.*, "DMD-based adaptive spectral imagers for hyperspectral imagery and direct detection

of spectral signatures," in *Emerging Digital Micromirror Device Based Systems and Applications,* L. J. Hornbeck and M. R. Douglass, eds. (SPIE, 2009).
25. E. Hemsley, I. Ardi, T. Rouvier, *et al*., "Fast reconstruction of hyperspectral images from coded acquisitions using a separability assumption," Opt. Express **30**, 8174–8185 (2022).
26. A. Parada-Mayorga and G. R. Arce, "Spectral super-resolution in colored coded aperture spectral imaging," IEEE Trans. on Comput. Imaging **2**, 440–455 (2016).
27. N. Monvoisin, E. Hemsley, L. Laplanche, *et al*., "Spectrally-shaped illumination for improved optical monitoring of lateral III-V-semiconductor oxidation," Opt. Express **31**, 12955 (2023).
28. E. Tseng, A. Mosleh, F. Mannan, *et al*., "Differentiable compound optics and processing pipeline optimization for end-to-end camera design," ACM Trans. on Graph. (TOG) **40** (2021).